

Terahertz quasi-perfect vortex beam with integer-order and fractional-order generated by spiral spherical harmonic axicon

Si-Yu Tu(涂思语), De-Feng Liu(刘德峰), Jin-Song Liu(刘劲松), Zhen-Gang Yang(杨振刚), and Ke-Jia Wang(王可嘉)
Citation: Chin. Phys. B, 2024, 33 (**1**): 014211. DOI: 10.1088/1674-1056/acf91c
Journal homepage: http://cpb.iphy.ac.cn; http://iopscience.iop.org/cpb

What follows is a list of articles you may be interested in

Multi-channel terahertz focused beam generator based on shared-aperture metasurface

Jiu-Sheng Li(李九生) and Yi Chen(陈翊)
Chin. Phys. B, 2023, 32 (**12**): 124204. DOI: 10.1088/1674-1056/acddd2

Terahertz shaping technology based on coherent beam combining

Xiao-Ran Zheng(郑晓冉), Dan-Ni Ma(马丹妮), Guang-Tong Jiang(蒋广通), Cun-Lin Zhang(张存林), and Liang-Liang Zhang(张亮亮)
Chin. Phys. B, 2023, 32 (**11**): 114210. DOI: 10.1088/1674-1056/acc2b0

Single-mode GaSb-based laterally coupled distributed-feedback laser for CO_2 gas detection

Shi-Xian Han(韩实现), Jin-Yi Yan(严进一), Chun-Fang Cao(曹春芳), Jin Yang(杨锦), An-Tian Du(杜安天), Yuan-Yu Chen(陈元宇), Ruo-Tao Liu(刘若涛), Hai-Long Wang(王海龙), and Qian Gong(龚谦)
Chin. Phys. B, 2023, 32 (**10**): 104205. DOI: 10.1088/1674-1056/accff2

High efficiency of broadband transmissive metasurface terahertz polarization converter

Qiangguo Zhou(周强国), Yang Li(李洋), Yongzhen Li(李永振), Niangjuan Yao(姚娘娟), and Zhiming Huang(黄志明)
Chin. Phys. B, 2023, 32 (**2**): 024201. DOI: 10.1088/1674-1056/ac6db7

Dual-function terahertz metasurface based on vanadium dioxide and graphene

Jiu-Sheng Li(李九生)† and Zhe-Wen Li(黎哲文)
Chin. Phys. B, 2022, 31 (**9**): 094201. DOI: 10.1088/1674-1056/ac5884

Terahertz quasi-perfect vortex beam with integer-order and fractional-order generated by spiral spherical harmonic axicon

Si-Yu Tu(涂思语)[1], De-Feng Liu(刘德峰)[2], Jin-Song Liu(刘劲松)[1], Zhen-Gang Yang(杨振刚)[1], and Ke-Jia Wang(王可嘉)[1,†]

[1] *Wuhan National Laboratory for Optoelectronics, School of Optical and Electronic Information, Huazhong University of Science and Technology, Wuhan* 430074, *China*

[2] *AVIC Beijing Changcheng Aeronautical Measurement and Control Technology Research Institute, Beijing* 101111, *China*

(Received 1 August 2023; revised manuscript received 31 August 2023; accepted manuscript online 13 September 2023)

We propose a new method to generate terahertz perfect vortex beam with integer-order and fractional-order. A new optical diffractive element composed of the phase combination of a spherical harmonic axicon and a spiral phase plate is designed and called spiral spherical harmonic axicon. A terahertz Gaussian beam passes through the spiral spherical harmonic axicon to generate a terahertz vortex beam. When only the topological charge number carried by spiral spherical harmonic axicon increases, the ring radius of terahertz vortex beam increases slightly, so the beam is shaped into a terahertz quasi-perfect vortex beam. Importantly, the terahertz quasi-perfect vortex beam can carry not only integer-order topological charge number but also fractional-order topological charge number. This is the first time that vortex beam and quasi-perfect vortex beam with fractional-order have been successfully realized in terahertz domain and experiment.

Keywords: terahertz, spiral spherical harmonic axicon, quasi-perfect vortex beam, topological charge number

PACS: 42.25.–p, 04.30.–w, 07.57.–c **DOI:** 10.1088/1674-1056/acf91c

1. Introduction

In recent years, optical vortex beams carried orbital angular momentum (OAM) have attracted much attention.[1–4] The OAM gives electromagnetic waves spiral phase characteristic in the plane perpendicular to the propagation direction, and making light intensity of the beams distributed in a circular ring ("doughnut") shape. The OAM of vortex beam has infinite modes (infinite topological charge number n), and modes are mutually orthogonal.[5] The topological charge number n can be an integer or a fraction, and the fractional vortex beam further carries more information. Therefore, the interactive crosstalk is reduced during transmission, and communication system capacity can be infinitely improved, theoretically. At present, vortex beams with integer and fractional topological charge number have been utilized in the fields of particle manipulation,[6–9] high-capacity and high-rate communication,[10–13] quantum information,[14,15] and super-resolution microscopy imaging.[16]

However, in practical applications, the ring radius of vortex beams increases rapidly as topological charge number increases, and gradually increases along the propagation direction. This characteristic causes difficulties in coupling multiple OAM modes of vortex beams into fixed-aperture fibers or waveguides. In 2013, Ostrovsky *et al*. first proposed the concept of a perfect vortex beam (PVB) whose ring radius does not vary with topological charge number.[17] In 2015, Vaity and Rusch performed Fourier transformation on Bessel–Gaussian beam generated by spiral axicon to form PVB at 1550 nm, whose ring radius slightly shifts with the increase of topological charge number.[18] Kotlyar *et al*. generated PVB by optimal phase elements and Fourier transformation lens, in 2016.[19]

Terahertz (THz) waves are intermediate in the electromagnetic spectrum between infrared radiation and microwave, so they have the characteristics of both fields. As the resources of traditional optical communication and microwave communication are gradually exhausted, THz communication with wideband has become a research hotspot.[20,21] THz vortex beam with high frequency is an ideal carrier for future wireless communications, and further enhances degrees of freedom. In 2014, Schemmel *et al*. used polyethylene material to fabricate spiral phase plate (SPP), and generated THz vortex beams at 0.1 THz, firstly.[22] In 2015, Wei *et al*. introduced high precision and low-cost three-dimensional (3D) printing technology to fabricate spiral axicon and SPP, generating arbitrary order Bessel beams and vortex beam at 0.3 THz.[23] In 2022, Wang *et al*. used a fractional-order vortex two-color field to generate THz fractional vortex beam in simulation.[24] Furthermore, it is demonstrated that THz vortex beams can be used in communication[20,25] and magnetic excitations.[26] Nevertheless, THz vortex beam has the same disadvantages as optical vortex beam in which ring radius increases with the topological charge number increasing. So, it is imperative to investigate the generation of PVB in the THz band. Currently, the available methods of generating THz PVB are very few. In 2020, Yang *et al*. adopted the method of optimal phase ele-

†Corresponding author. E-mail: wkjtode@sina.com

© 2024 Chinese Physical Society and IOP Publishing Ltd

ments and Fourier transformation lens in visible light to generate THz PVB at 0.1 THz, but the utilization of two elements for generating vortex beam increases optical path and reduces the power of beam, which is not conducive to the integration of system.[27] In 2022, Liu *et al*. proposed multi-functional metasurfaces to generate THz quasi-perfect vortex beam (QPVB) with a small divergence angle, whose ring radius vary slightly with topological charge number, however, this method is limited by the geometric phase theory, and the fabrication process is complex and costly.[28] In 2023, Huang *et al*. proposed an all-dielectric metasurface to generate superimposed THz PVB, which is suitable for ultra-miniature functional devices.[29] To the best of our knowledge, there has been no experimentally fractional vortex beam and perfect fractional vortex beam generated in THz domain.

In this paper, we propose a spiral spherical harmonic axicon (SSHA) for generating THz QPVB with integer-order and fractional-order. Only a single diffractive element is capable of transforming Gaussian beam into vortex beam with integer-order or fractional-order, and the ring radius of vortex beam slightly increases with the topological charge number increasing, so we call it THz QPVB. The THz QPVB with integer-order and with fractional-order have been successfully generated at 0.1 THz numerically and experimentally, and the ring radius varies little in a propagation distance of at least 50 mm. Modifying the spherical harmonic coefficient (SHC) of SSHA has the ability to keep ring radius constant despite variation of topological charge number, thus realizing the property of PVB. Moreover, the manufacturing method with 3D printing method is simple, high-precision and low-cost. These advantages hold significant application value for coupling vortex beam into fixed-aperture fibers or waveguides. In addition, the OAM state carried by QPVB is verified by a focusing hyperbolic (FH) lens,[30] proving its vortex nature.

2. Design process, simulation and fabricating

2.1. Design process

The optical element spherical harmonic axicon (SHA) was proposed to generate long-distance THz zero-order diffraction-free beam in 2022,[31] and the SHC l mainly determines surface shape of SHA. In this study, the phase of SHA and spiral phase plate (SPP) are combined to form a new optical phase element, we refer to the new phase element as SSHA. Next, the design process of phase of SSHA is introduced.

The SHA composed of spherical harmonic function curve and traditional axicon has been detailed in Ref. [28], where the base angle, diameter, SHC, thickness and refractive index of SHA are denoted by base angle γ, $2R$, l, $d_1(r)$, and n_1 respectively, as shown in Fig. 1. The γ and l are both larger, the SHA is thicker. The phase plane of SHA is

$$\phi_{\mathrm{SHA}} = n_1 k d_1(r), \tag{1}$$

where $k = 2\pi/\lambda$ is the wave number and λ is the wavelength.

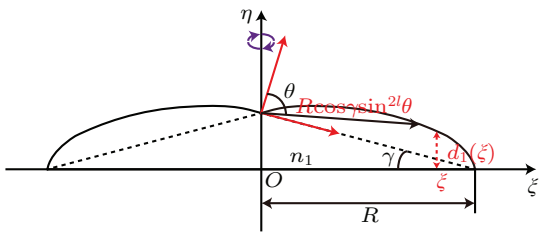


Fig. 1. The two-dimensional (2D) cross section of SHA.

The phase plane of SPP is

$$\phi_{\mathrm{SPP}} = n\varphi, \tag{2}$$

where n denotes the topological charge number, φ is the azimuthal angle ranging from 0 to 2π.

Since the SSHA is a combination of phase of SPP and SHA, the phase plane of SSHA is given by

$$\phi_{\mathrm{SSHA}} = \phi_{\mathrm{SHA}} + \phi_{\mathrm{SPP}} = n_1 k d_1(r) + n\varphi. \tag{3}$$

The phase of SSHA is wrapped 2π to form diffractive element, which can reduce thickness and power-loss, and it is expressed as

$$\phi_{\mathrm{SSHA}} = \mathrm{mod}\left(\phi_{\mathrm{SSHA}}, 2\pi\right). \tag{4}$$

The above content describes the design process of phase of SSHA.

2.2. Simulation

2.2.1. Generation of QPVB with integer-order

The phase formation process of SSHAs with a base angle $\gamma = 10^\circ$, SHC $l = 10$, topological charge number n in a range from -2 to 2 are given in Fig. 2, the first row, the second row, and the third row show the phase distributions of SHA, SPPs, and SSHAs with different values of topological charge number n respectively. In the figure, the refractive index n_1 is 1.645, the wavelength λ is 3 mm, the base angle γ is 10°, and the diameter $2R$ is 101.6 mm. Based on these parameters, the phase ϕ_{SSHA} of SSHA can be calculated. In addition, when the topological charge number n is zero, the phase of SHA and SSHA are identical with each other.

For a THz Gaussian beam $E_0 = \exp\left(-r^2/w_0^2\right)$ with a waist radius $w_0 = 27$ mm passing through SSHAs, based on the phase modulation theory of the lens,[32] the output scalar electric field is given by

$$E_{\mathrm{out}} = \exp\left(-\frac{r^2}{w_0^2}\right)\exp\left(\mathrm{i}\phi_{\mathrm{SSHA}}\right). \tag{5}$$

Based on angular spectrum theory (AST), i.e., Eqs. (3) and (4), the output beams behind SSHAs can be easily obtained by matlab software. Figures 3(a)–3(c) show the output beams

generated by SSHAs, and the x–z planes of output beams are shown in Figs. 3(a1)–3(a5). It can be seen that vortex beams with different values of topological charge number n are initially formed behind phase elements, and the ring-radius of the beam does not change visually along the propagation direction in a range from $z = 75$ mm to $z = 125$ mm. As the propagation distance increases, the vortex beams degenerate into corresponding order diffraction-free beams at about $z = 175$ mm. Figures 3(b1)–3(b5) display the intensity distributions of x–y plane of output beams with different values of topological charge number n at $z = 100$ mm, visually indicating that the sizes of vortex beam with different values of topological charge number n have no variation. At $z = 300$ mm, the intensity distributions in the x–y plane of the beams have Bessel-like beams with different orders, in Figs. 3(c1)–3(c5). Furthermore, the intensity distributions of two beams generated by two SSHAs carrying the same absolute value of topological charge but opposite signs are identical with each other. Then, the ring radiuses of vortex beam in a range from $z = 75$ mm to $z = 125$ mm are shown in Figs. 3(d1)–3(d5). It can be observed that the ring radiuses of vortex beam with different values of topological charge number n vary little along the propagation direction. The average values of ring radius of vortex beams along $z = 75$ mm to $z = 125$ mm with n from -2 to 2 are 18.38 mm, 17.38 mm, 16.76 mm, 17.38 mm, and 18.38 mm respectively. The ring radius is shifted by 3.57% for adding one topological charge, so the vortex beam generated by SSHA is QPVB.

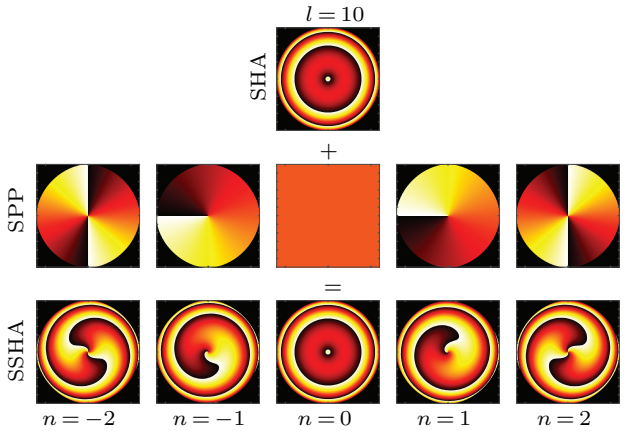


Fig. 2. Phase formation process of SSHAs (the first row, the second row, and the third row show the phase distributions of SHA with a base angle $\gamma = 10°$, SHC $l = 10$, SPPs, and SSHAs for different values of topological charge number n).

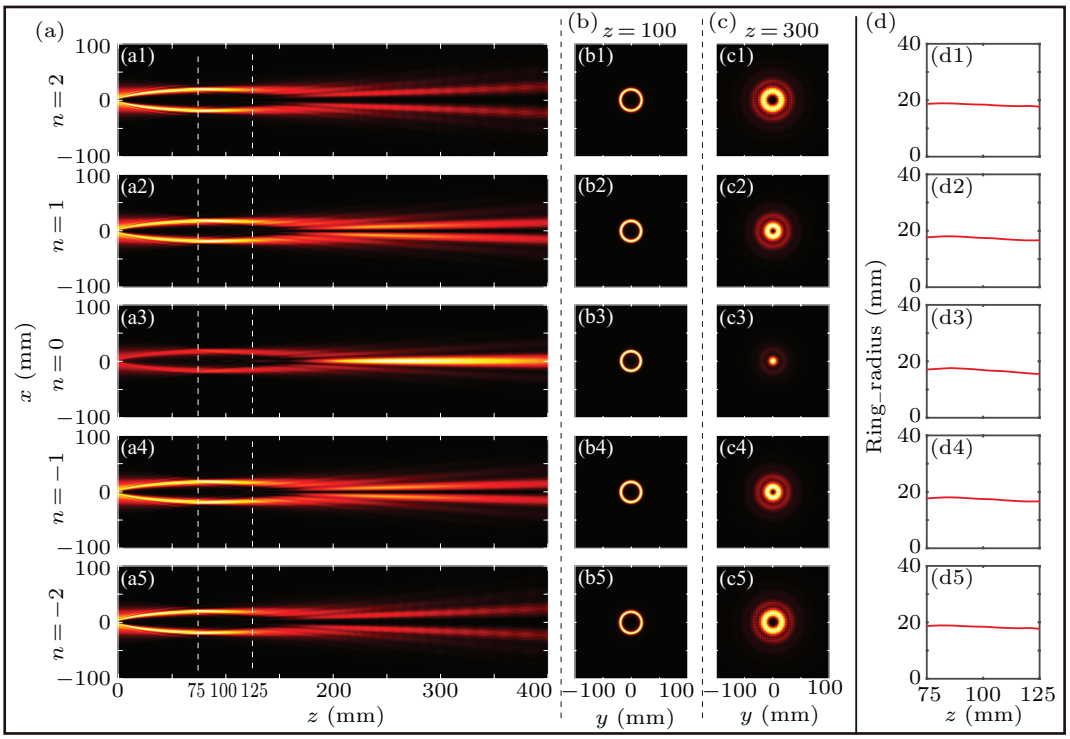


Fig. 3. (a) The x–z plane of output beams and (b) x–y plane of output beams at position $z = 100$ mm, (c) x–y plane of output beams at position $z = 300$ mm, (d) ring radiuses of vortex beam at propagation direction ranging from $z = 75$ mm to $z = 125$ mm (the first row to the five row correspond to simulation results of SSHAs with $\gamma = 10°$, $l = 10$, n ranging from -2 to 2 respectively).

The FH lens proposed by Yang *et al.*[30] have been used to verify vortex property of the beam generated by SSHA, and the method proposed in Ref. [31] can also detect topological charge number.[33] The parameter α and focal length f of FH lens are set to 4×10^{-3} and 100 mm respectively, and the phase of FH lens is displayed in Fig. 4(a). When the beam passes through FH lens, a diffraction pattern can be obtained in focal plane of the FH lens. The value of topological charge number n is estimated by the diffraction fringe number. Figures 4(b1)–4(b5) show diffraction patterns of QPVB with topological charge number n from -2 to 2 converted by FH lens. For topological charge number $n \neq 0$, the two ends

of diffraction fringes are two bright spots, while in the middle are fringes of light and dark. There are n dark fringes and $n+1$ bright spots, and the direction between two bright spots is determined by the positive value or negative value of n. For topological charge number $n = 0$, the center of diffraction pattern is a bright spot. This simulation result indicates that the QPVB generated by SSHA carries OAM states and has vortex property.

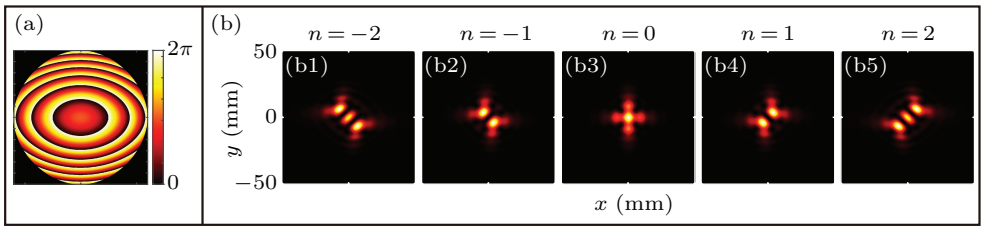


Fig. 4. (a) Phase of FH lens, (b) distributions of diffraction pattern by FH lens, with panels (b1)–(b5) corresponding to different values of topological charge number n.

The above research contents mainly aim at the same SHC $l = 10$, and different values of topological charge number n. Moreover, the influences of SSHAs with different values of SHC l on QPVB are investigated, which is important to achieve the property of PVB. We mainly calculate the output beams generated by Gaussian beam passing through SSHAs with a base angle $\gamma = 10°$, SHC $l = 1$, $l = 5$, $l = 10$, and $l = 20$. It can be seen from Ref. [28] that the SHC is larger, the thickness values of both sides of SHA are larger. Therefore, the variations of phase are greater on both sides, and the ring radius is larger. For example, we show the phase of SSHA with $n = 2$ and different SHCs in Fig. 5(a). In Figs. 5(b)–5(d), the intensity distributions of x–y plane of beams generated by SSHAs with SHC $l = 5$, $l = 10$, and $l = 20$, variations of topological charge number n from -2 to 2 at $z = 100$ mm are shown. For $l = 5$, the size of vortex beam does not change visually as shown in Fig. 5(b). For $l = 10$, the size of vortex beam becomes slightly larger with the increase of topological charge number n as shown in Fig. 5(c). For $l = 20$, the size of vortex beam changes more obviously with the increase of topological charge number n (see Fig. 5(d)). The variations of ring radius of QPVB are given in Fig. 5(e), where QPVB with $l = 5$, $l = 10$, and $l = 20$ are denoted by red line, yellow line, and purple line, the ring radius is shifted by 1.03%, 3.63%, and 8.93% for adding one topological charge, respectively. It is indicated that the SHC l is smaller, the ring radius increases more slowly with the increase of topological charge number. Theoretically, when $l = 1$, the change ratio of ring radius is the lowest, so the beams generated by SSHAs with $n = 0$ and $n = 10$ are calculated (see Fig. 5(f)). The ring radiuses are 23.20 mm and 24.95 mm, which is shifted by 0.70% by adding one topological charge on average. Notably, when the SHC l of SSHA is larger, the ring radius of vortex beam is smaller for the same topological charge number n, and more obviously affected by changing topological charge number. The SHC l can be any positive integer, so the ring radius of vortex beam has a large adjustable range. Based on these characteristics, it is possible to keep the ring radius invariant with the variation of topological charge number n by controlling SHC l, which can achieve the property of PVB.

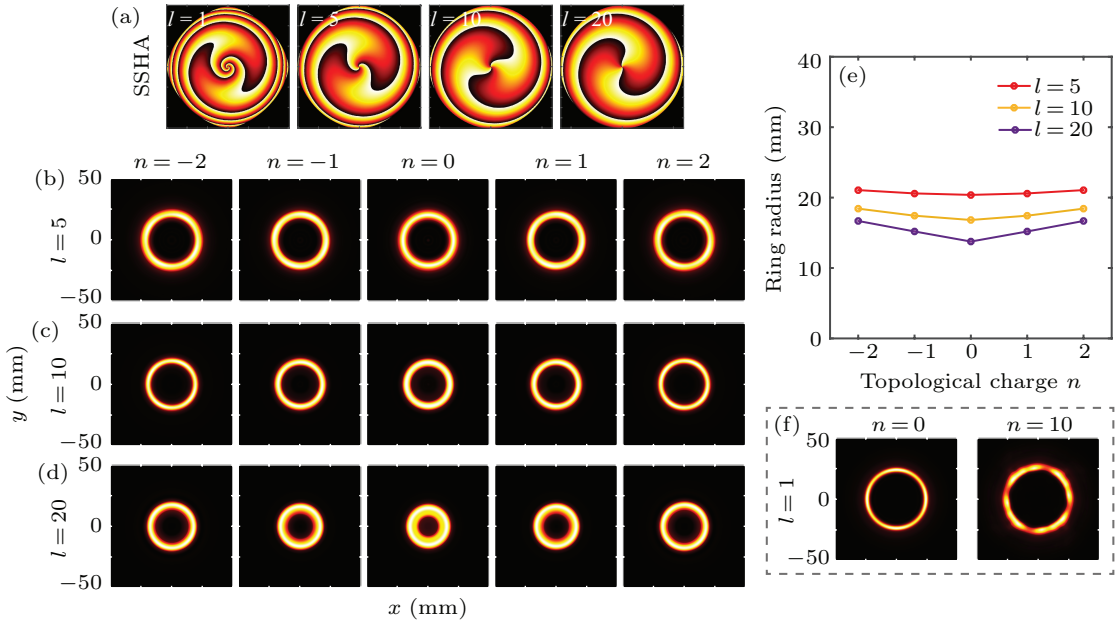


Fig. 5. (a) Phase distributions of SSHAs with $n = 2$, $l = 1$, $l = 5$, $l = 10$, and $l = 20$, intensity distribution of x–y plane of QPVB generated by SSHA with $l = 5$ (b), 10 (c), and 20 (d) at $z = 100$ mm, with topological charge number n varying from -2 to 2; (e) ring radius of QPVB with different values of SHC l and of topological charge number n, (f) x–y plane of QPVB generated by SSHA with $l = 1$, $n = 0$, and $n = 10$.

2.2.2. Generation of QPVB with fractional-order

In Subsection 2.2.1, the QPVB generated by SSHA with integer topological charge number are studied. Here, we explore fractional vortex beam generated by SSHA carrying fractional topological charge number at 0.1 THz. Likewise, according to angular spectrum theory and its transmission function, the beams generated by a Gaussian beam passing through SSHA which possesses fractional topological charge number n (0.2, 0.5, 0.8, 2.2, 2.5, 2.8) and SHC $l = 10$ are calculated.

It can be observed that the phases of SSHAs have a sense of separation while the topological charge number is fractional in Fig. 6(a), the difference of topological charge is only 0.2 or 0.3 whose phase distribution has an apparently change. Looking at the intensity distribution of x–y plane in Fig. 6(b), the vortex beam with fractional-order is in the shape of a "doughnut" with radial notch, furthermore, the fractional part of fractional topological charge number is closer to a half-integer, the notch is more obvious. Importantly, the size of vortex beams appears to be approximately the same visually. Subsequently, we have calculated in detail the ring radiuses of vortex beams with fractional-order. The results are displayed in Fig. 6(c), blue dots and red dots represent the ring radius of n charges from 0.2 to 0.8 and from 2.2 to 2.8, respectively. The ring radius of vortex beams generated by SSHAs changes slightly with the increase of topological charges. And the ring radiuses of fractional vortex beams with $n = 0.2$, $n = 0.5$, $n = 0.8$ are shifted by 9.02%, 9.83%, 7.68% relative to fractional vortex beams with $n = 2.2$, $n = 2.5$, $n = 2.8$, respectively. Therefore, SSHA can generate a QPVB with fractional-order at 0.1 THz.

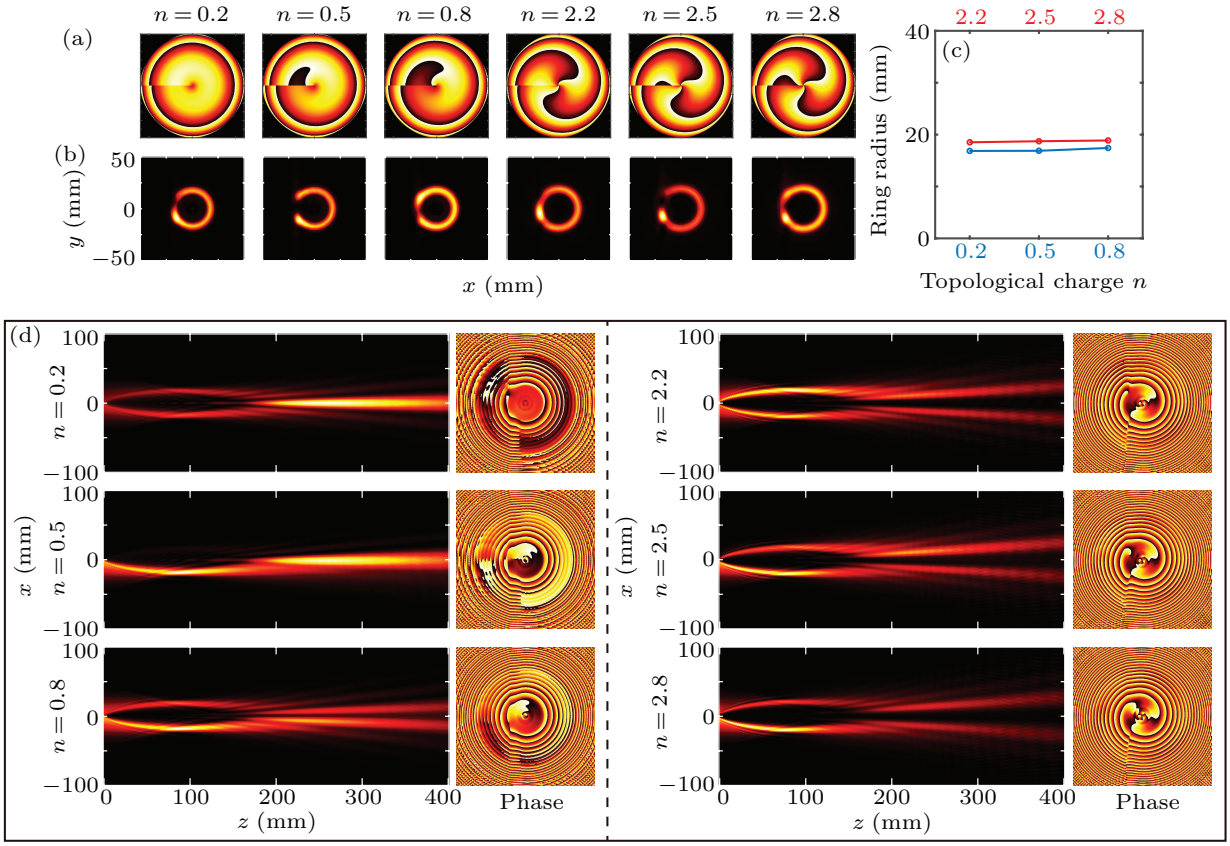


Fig. 6. (a) The phase and (b) the intensity distribution of x–y plane of vortex beams generated by SSHA with fractional-order, (c) ring radius with topological charge number n, and (d) intensity distribution of x–z plane and phase distribution of x–y plane at $z = 100$ mm.

Figure 6(d) shows the intensity distribution of x–z plane. Its topological charge number n is 0.2 or 2.2, and the intensity distribution is very similar to the counterpart of integer-order, with symmetry in the x direction. Its topological charge n is 0.5 or 2.5, the intensity distribution is no longer symmetrical in the x direction. When topological charge n increases to 0.8 or 2.8, the asymmetry in the x direction is relatively weakened. In addition, the phase distribution of QPVB with fractional-order at $z = 100$ mm is given in Fig. 6(d), it can be seen that the phase distribution has a split due to the topological charge n with fractional-order.

2.3. Fabricating

According to the principle of equal optical path, when a beam passes through a homogeneous medium, the phase shifting is $\phi = 2\pi(n_1 - 1)h/\lambda$, n_1 and h are the refractive index and thickness of homogeneous medium, respectively. In order to avoid zero thickness of element, the base thickness $h_0 = 2$ mm is added to bottom surface of the diffractive element.

Therefore, the height distribution of SSHA can be expressed as

$$h_{\mathrm{SSHA}} = \frac{\lambda}{2\pi(n_1 - 1)}\phi_{\mathrm{SSHA}} + h_0. \tag{6}$$

According to Eq. (6), the height distribution of SSHA is calculated, in which the maximum height of element is 6.65 mm. So, the 3D model of diffractive element SSHA can be obtained by height distribution, and its stereolithography file is acquired based on matlab software. The 3D model of SSHA with integer-order and fractional-order are displayed in Fig. 7. In addition, the FH lens with $2R = 101.6$ mm, $\alpha = 4 \times 10^{-3}$, and $f = 100$ mm is fabricated. The 3D printing technology is employed to fabricate SSHA by importing the 3D models into a 3D printer (Lite450HD, UnionTech, Leyi3D) which takes an advantage of high precision and low cost. The refractive index n_1 of the polymer 3D printing material is about 1.645 at 0.1 THz. The transverse and longitudinal printing precision of this 3D printer are 42 μm and 28 μm, respectively.

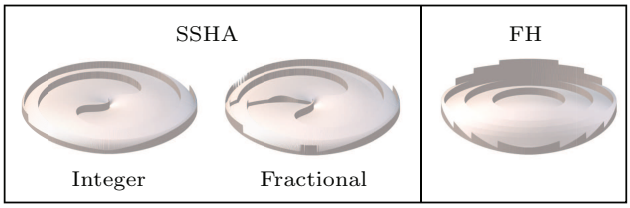


Fig. 7. The 3D model of SSHA and FH lens.

3. Experiment

3.1. Experimental setup

The schematic diagram of experimental setup is shown in Fig. 8. The 0.1-THz source is an InP Gunn diode coupled by a horn antenna (GKa-100, SPACEK LABS), which emits a divergent Gaussian beam. The divergent Gaussian beam is transformed into a collimated Gaussian beam with a waist radius $\omega = 27$ mm by using a lens with a focal length f of 100 mm. Then, the collimated Gaussian beam passes through SSHA. The FH lens is placed $d = 100$ mm behind SSHA to detect topological charge number n. Finally, the THz detector is a broadband high sensitivity Schottky diode mounted on a 3D translation stage to measure beams. The scanning range of the x direction and y direction are both from -100 mm to 100 mm with an interval of 1 mm, and the scanning range of z direction is from 0 mm to 400 mm with an interval of 2 mm.

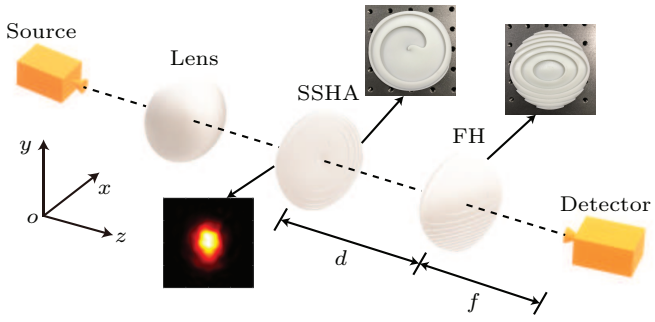


Fig. 8. Schematic diagram of experimental setup.

3.2. Experimental results

The intensity distributions of beams generated by SSHA with $\gamma = 10°$, $l = 10$, topological charge number n from -2 to 2 in experiment are shown in Figs. 9(a) and 9(b). Like simulation results, the THz Gaussian beam passing through SSHA is transformed into a vortex beam propagation about 200 mm firstly, and the ring radius of vortex beam does not vary visually with the topological charge number n in Figs. 9(a1)–9(a5). Then, the intensity distribution of x–z plane shows that the ring radius of vortex beam visually varies very little from $z = 76$ mm to $z = 200$ mm in the propagation direction. Finally, the vortex beam degenerates into a diffraction-free beam of corresponding order, the intensity distributions in x–y plane at $z = 300$ mm are shown in Figs. 9(b1)–9(b5). Because of the uneven intensity distribution of Gaussian beam incident on SSHA and the absorption of intensity by material of SSHA, the intensity distribution of vortex beam and diffraction beam are not so even as simulation results. It can be observed that the x directions of relative strongest intensities are opposite in sign. We calculate the ring radiuses of vortex beams with different values of topological charge number in a range from $z = 76$ mm to $z = 200$ mm, which vary slightly (see Figs. 9(c1)–9(c5)). The average values of ring radius with topological charge number from -2 to 2 are 24.58 mm, 23.97 mm, 23.77 mm, 23.54 mm, 24.52 mm, which shift very little. The experimental result illustrates that the vortex beam generated by SSHA is QPVB.

For proving the vortex property of QPVB generated by SSHA, the FH lens is utilized. The experimental setup is shown in Fig. 8, the FH lens is placed $d = 100$ mm behind SSHA, the detector is placed $f = 100$ mm behind FH lens along the propagation direction. At focal plane, the intensity distribution of beams in the x–y plane is detected, and the detection range is 100 mm×100 mm. In Figs. 9(d1)–9(d5), the intensity distributions of QPVB with $l = 10$ and different n values passing through FH lens are detected. For topological charge number $n = 0$, the diffraction pattern has a bright spot in the center. For topological charge number $n \neq 0$, it can be observed that $n + 1$ bright spots with n dark fringes are generated in the diffraction pattern. The number of dark fringes between bright spots is equal to topological charge number n of designed SSHA. This experimental result verifies the vortex nature of QPVB generated by SSHA.

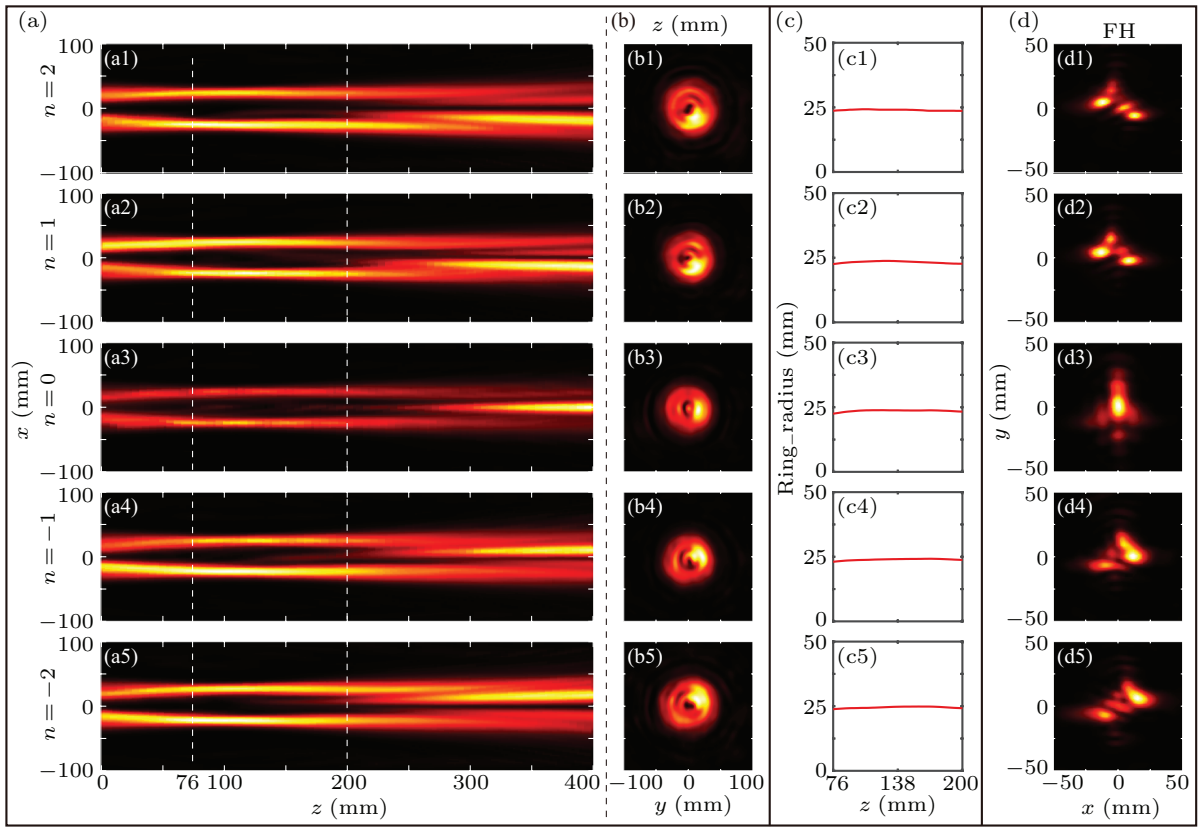


Fig. 9. (a) The x–z plane of output beams and (b) x–y plane of output beams at position $z = 300$ mm, (c) ring radius of vortex beam in propagation direction from $z = 76$ mm to $z = 200$ mm, (d) FH lens detecting QPVB, with the first row to the five row corresponding to experimental results of SSHAs with $\gamma = 10°$, $l = 10$, n from -2 to 2 respectively.

Furthermore, we collect the vortex beam generated by SSHAs with SHC $l = 5$, $l = 10$, and $l = 20$, with topological charge number n varying from -2 to 2, at the position 100 mm behind SSHA. Figures 10(a)–10(c) show the intensity distribution of x–y plane of beam generated by SSHA at $z = 100$ mm. It can be seen that the intensity distributions are all in the shape of circular ring, and the size of the vortex beam varies slightly with the topological charge number n when the value of SHC l is fixed. The size of the vortex beam generated by SSHA in the experiment is larger than the value with corresponding SHC l and topological charge number n in simulation. These differences may be due to the scattering of phase element and the error of experimental system (for example, the spot of quasi-Gaussian beam incident on SSHA is rough). The ring radius of vortex beam is calculated and displayed in Fig. 10(d), the red line, yellow line, and purple line denote SSHA with $l = 5$, $l = 10$, and $l = 20$ respectively. For SSHA with $l = 5$, in the case that the topological charges are the same in number but opposite in sign, the ring radiuses are the same, which is consistent with the simulation result. Additionally, the ring radiuses are basically the same when the topological charge number $n = 0$ and $n = \pm 1$. While the topological charge number increases from $n = \pm 1$ to $n = \pm 2$, the ring radius is shifted by 1.86%. Like the SSHA with $l = 5$, the ring radiuses of vortex beam generated by SSHA with $l = 10$ are the same when topological charge number $n = 0$, ± 1. The ring radius is shifted by 2.09% while topological charge number $n = \pm 1$ increases to $n = \pm 2$. For SSHA with $l = 20$, the ring radius is smallest with topological charge $n = 1$, which may be caused by experimental errors. Next, the ring radius is shifted by 2.39% when topological charge number increases from $n = 0$ to $n = -1$, and the ring radius is shifted by 6.96% when topological charge number increases from $n = -1$ to $n = -2$. The intensity distributions of vortex beam generated by SSHA with $l = 1$, $n = 0$, and $n = 10$ are shown in Fig. 10(e). The ring radiuses are 25.87 mm and 27.23 mm respectively, each of which is shifted by 0.50% by adding one topological charge on average. The beam generated by SSHA increases slightly with the topological charge number n increasing, which is consistent with simulation result, demonstrating that SSHA can generate QPVB in practical application. In addition, as the value of l becomes larger, the ring radius of the beam generated by SSHA turns smaller, and the shift with the increase of topological charge number n becomes more significant. Therefore, the ring radius can be kept invariant by controlling SHC l to realize property of PVB.

Next, the beams generated by Gaussian beam passing through SSHA with $l = 10$, $n = 0.2$, 0.5, 0.8, 2.2, 2.5, 2.8 are measured in experiment. Like the simulation results, the "doughnut" shape beams with radial notch are generated as shown in Fig. 11(a), when the fraction is 0.5, the radial notch is most noticeable. When the topological charge n increases

by two, the size of vortex beam only slightly increases visually. The ring radius of vortex beam is calculated and the result is displayed in Fig. 11(b). When topological charge number $n = 0.2$, 0.5 or $n = 2.2$, 2.5, the ring radiuses are the same. When the fraction increases to 0.8 or 2.8, the ring radius of vortex beam increases slightly. The ring radiuses of fractional vortex beams with $n = 0.2$, $n = 0.5$, $n = 0.8$ are shifted by 6.14%, 6.14%, 9.60% relative to fractional vortex beams with $n = 2.2$, $n = 2.5$, $n = 2.8$. This experimental result shows that the SSHA successfully generates QPVB with fractional-order in experiment. In addition, the intensity distributions of x–z plane of the fractional vortex beam generated by SSHA are shown in Fig. 11(c).

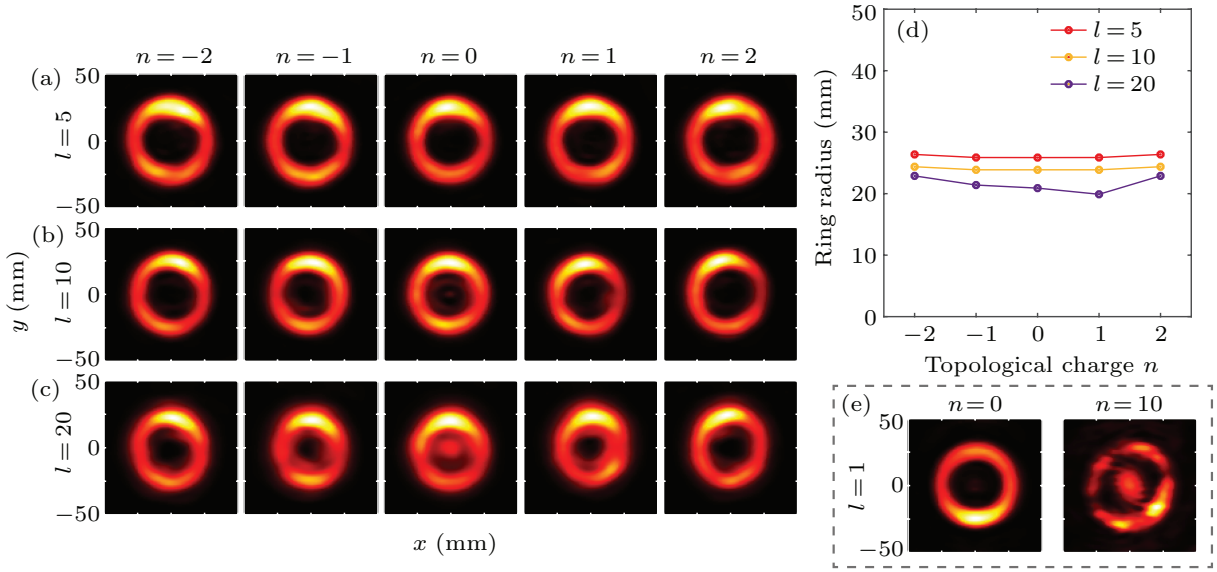


Fig. 10. The intensity distribution of x–y plane of QPVB generated by SSHA with $l = 5$ (a), 10 (b), and 20 (c) at $z = 100$ mm, with topological charge number n varying from -2 to 2; (d) ring radiuses of QPVB with different values of SHC l and topological charge number n, (e) x–y plane of QPVB generated by SSHA with $l = 1$, $n = 0$, and $n = 10$.

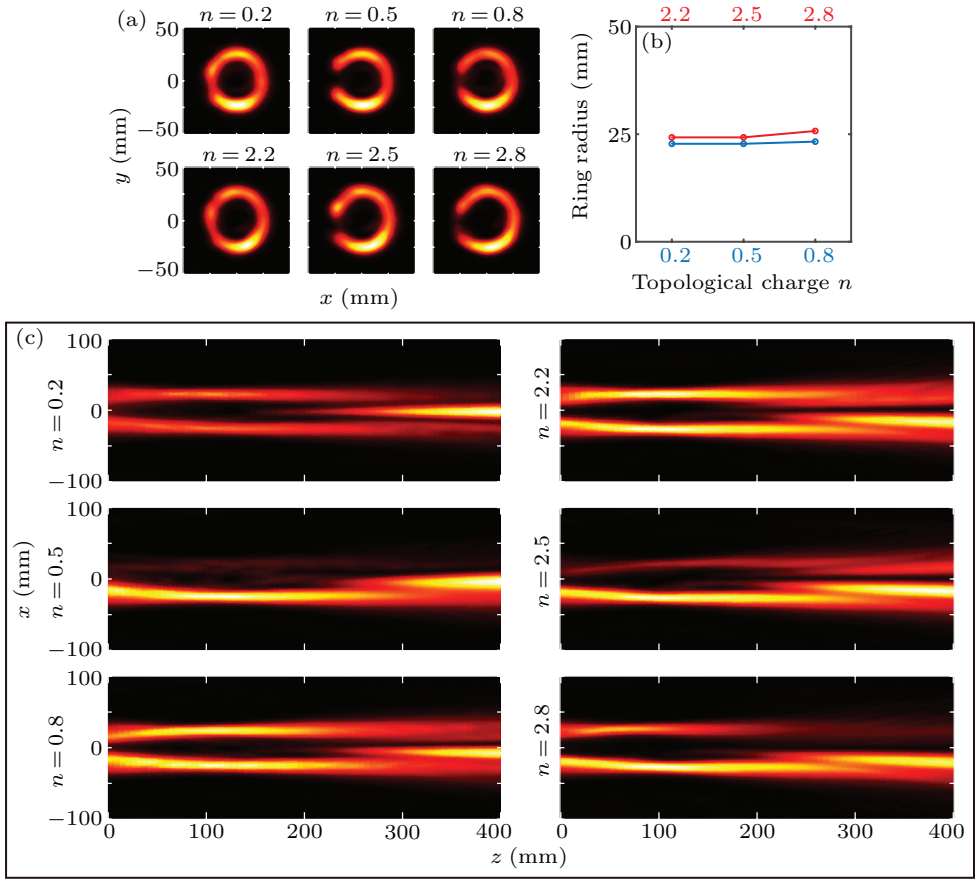


Fig. 11. (a) Intensity distributions of x–y plane of vortex beams generated by SSHA with fractional-order, (b) ring radiuses with different values of topological charge number n, and (c) intensity distributions of x–z plane.

4. Discussion

4.1. Comparison between SSHA and SPP

The traditional method uses SPP to generate a Laguerre–Gaussian (LG) beam whose ring radius increases with topological charge number n. In order to compare with the SSHA, the LG beams generated by SPPs with $n = 0$, 1, 2, 3 are calculated by AST. The ring radius of LG beams with different values of topological charge number n at $z = 100$ mm is calculated, which is denoted by blue line in Fig. 12(a), and the intensity distributions of x–y plane are shown in Fig. 12(b). For comparison, the ring radius of the QPVB generated by SSHA with $l = 10$ is denoted by red line in Fig. 12(a).

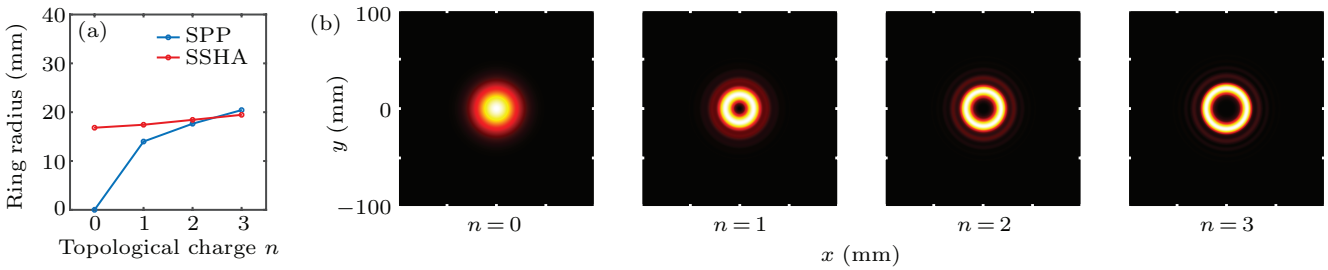


Fig. 12. (a) Variations of ring radius with topological charge number n for SPP and SSHA, and (b) intensity distributions of x–y plane of LG beam at $z = 100$ mm.

It can be observed that the ring radius varies most when the topological charge number n of SPP increases from 0 to 1. While the topological charge number $n$increases linearly from 1 to 3, and the growth rate of ring radius is obviously higher than that of SSHA. For $n < 2$, the ring radius of the LG beam generated by SPP is smaller than that of the QPVB generated by SSHA. For $n = 2$, the two components are closest. When the topological charge number n exceeds 2, the ring radius of the LG beam generated by SPP is larger than that of the QPVB generated by SSHA. The ring radiuses of LG beam generated by SPP with $n = 0$, 1, 2, 3 at $z = 100$ mm are 0 mm, 13.99 mm, 17.64 mm, 20.43 mm respectively.

4.2. Limit to topological charge number

The SSHA has an upper limit to the topological charge number n, when the ring radius is kept unchanged. From the previous research results, the ring radius increases slightly with the augment of the topological charge number n when the SHC l is unchanged, and decreases with the SHC l increasing when the topological charge number n is unchanged. The minimum value of the SHC l is 1, and the ring radius of vortex beam with $l = 1$ and $n = 0$ is 23.20 mm. In order to explore the limit to the topological charge number n carried by SSHA under the condition that the ring radius is basically unchanged, SHC l and topological charge number n need increasing. Firstly, the SHC l is set to 20, and the ring radius of vortex beam with $n = 40$ is 23.01 mm, which is almost close to 23.20 mm, when the topological charge number n exceeds 40, the ring radius is greater than 23.20 mm. Then, the SHC l is set to 40, the ring radius of the vortex beam with $n = 40$ is 22.98 mm, which is slightly different from SSHA with $l = 20$. The influence on ring radius with $n = 40$ is small when the SHC l exceeds 20. The above discussion shows that the upper limit to the topological charge is $n = 40$. Adjusting the SHC l can keep the ring radius almost unchanged in the range of $n = 0, \ldots, 40$, but the corresponding z position will also move forward. Figure 13 shows the intensity distributions of x–y plane of the vortex beam generated by SSHAs with $l = 1$, $n = 0$, $l = 20$, $n = 40$, and $l = 40$, $n = 40$.

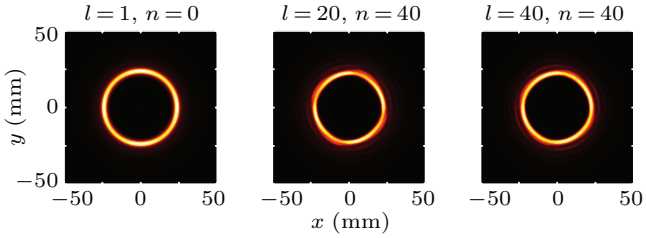


Fig. 13. Intensity distributions of x–y plane.

5. Conclusions and perspectives

In conclusion, we have designed a new optical diffractive phase element to generate a quasi-perfect vortex beam with integer-order and fractional-order topological charge number at 0.1 THz. The optical phase element is characterized by a new spherical harmonic axicon with an added spiral phase wavefront. Next, the phase of diffractive element is wrapped to 2π, which is fabricated by 3D printing technology with high precision at low cost. Both the theoretical calculations and the experimental results demonstrate that the ring radius of the THz vortex beam with integer-order and fractional-order generated by SSHA with the same spherical harmonic coefficient increase slightly with the increase of topological charge number in free space. In addition, by controlling spherical harmonic coefficient, the beams generated by SSHA with different topological charge numbers have the properties of THz perfect vortex beam, which can be efficiently coupled to fixed-aperture THz waveguide. The stable implementation and transmission of terahertz vortex beams in free space further promotes the improving of the communication capacity

in terahertz domain. This simple and effective design method can also be extended beyond THz band. Therefore it is necessary to seek for suitable fabricating methods and material whose 3D printing technology is difficult to fabricate component used in high frequency band.

Acknowledgement

Project supported by the Fundamental Research Funds for the Central Universities, China (Grant No. 2017KFYXJJ029).

References

[1] Allen, Beijersbergen, Spreeuw and Woerdman 1922 *Phys. Rev. A* **45** 8185
[2] Soskin M S, Gorshkov V N, Vasnetsov M V, Malos J T and Heckenberg N R 1997 *Phys. Rev. A* **56** 4064
[3] Wang X W, Nie Z Q, Liang Y, Wang J, Li T and Jia B H 2018 *Nanophotonics* **7** 1533
[4] Xie Z M and Zhang R X Forbes A, Oliveira M and Dennis M R 2021 *Nat. Photon.* **15** 253
[5] Yao A M and Padgett M J 2011 *Adv. Opt. Photon.* **3** 161
[6] Curtis J E and Grier D G 2003 *Phys. Rev. Lett.* **90** 133901
[7] Gahagan K T and Swartzlander G A 1996 *Opt. Lett.* **21** 827
[8] Marzo A, Caleap M and Drinkwater B W 2018 *Phys. Rev. Lett.* **120** 044301
[9] Marzo A, Caleap M and Drinkwater B W Tao S H, Yuan X C and Lin J 2005 *Opt. Express* **13** 7726
[10] Yan Y, Xie G D, Lavery M P J, Huang H, Ahmed N, Bao C J, Ren Y X, Cao Y W, Li L, Zhao Z, Molisch A F, Tur M, Padgett M J and Willner A E 2014 *Nat. Commun.* **5** 4876
[11] Wang J, Yang J Y, Fazal I M, Ahmed N, Yan Y, Huang H, Ren Y X, Yue Y, Dolinar S, Tur M and Willner A E 2016 *Nat. Commun.* **6** 488
[12] Wang J 2018 *Photon. Res.* **4** B14
[13] Zhang X H, Xia T, Cheng S B and Tao S H 2019 *Opt. Commun.* **431** 238
[14] Teja G P, Simon C and Goyal S K 2021 *Phys. Rev. A* **104** 043713
[15] Wallraff A, Lukashenko A, Lisenfeld J, Kemp A, Fistul M V, Koval Y and Ustinov A V 2003 *Nature* **425** 155
[16] Chen R, Agarwal K, Sheppard C J R and Chen X D 2013 *Opt. Lett.* **38** 3111
[17] Ostrovsky A S, Rickenstorff-Parrao C and Arrizon V 2013 *Opt. Lett.* **38** 534
[18] Vaity P and Rusch L 2011 *Opt. Lett.* **40** 597
[19] Kotlyar V V, Kovalev A A and Porfirev A P 2016 *J. Opt. Soc. Am.* **33** 2376
[20] Koenig S, Lopez-Diaz D, Antes J, Boes F, Henneberger R, Leuther A, Tessmann A, Schmogrow R, Hillerkuss D, Palmer R, Zwick T, Koos C, Freude W, Ambacher O, Leuthold J and Kallfass I 2013 *Nat. Photon.* **7** 977
[21] Akyildiz I F, Han C, Hu Z F, Nie S and Jornet J M 2022 *IEEE Trans. Commun.* **70** 4250
[22] Schemmel P, Pisano G and Maffei B 2014 *Opt. Express* **22** 14712
[23] Wei X L, Liu C M, Niu L T, Zhang Z Q, Wang K J, Yang Z G and Liu J S 2015 *Appl. Opt.* **54** 10641
[24] Wang H G, Xu S X, Chen Y Y and Shen B F 2022 *New J. Phys.* **24** 083027
[25] Troha T, Ostatnický T and Kužel P 2021 *Opt. Express* **29** 30461
[26] Sirenko A A, Marsik P, Bernhard C, Stanislavchuk T N, Kiryukhin V and Cheong S W 2019 *Phys. Rev. Lett.* **122** 237402
[27] Yang Y Q, Ye X, Niu L T, Wang K J, Yang Z G and Liu J S 2020 *Opt. Express* **28** 1417
[28] Liu W Y, Yang Q L, Xu Q, Jiang X H, Wu T, Gu J Q, Han J G and Zhang W L 2022 *Nanophotonics* **11** 3631
[29] Huang F, Yang Q L, Xu Q, Jiang X H, Wu T, Gu J Q, Han J G and Zhang W L 2023 *Photon. Res.* **11** 431
[30] Yang Y Q, Xu Q, Liu W Y, Wu T, Gu J Q and Liu J S 2020 *Appl. Opt* **59** 4685
[31] Tu S Y, Peng J Y, Yang Z G, Liu J S and Wang K J 2022 *Opt. Express* **30** 39976
[32] Lv N G 2016 *Fourier Optics* pp. 120–125
[33] Liu Y, Zhou C X, Guo K L, Wei Z C and Liu H Z 2020 *Opt. Express* **31** 16192